

See discussions, stats, and author profiles for this publication at: <https://www.researchgate.net/publication/283729703>

# Optical Properties of Photovoltaic Organic-Inorganic Lead Halide Perovskites

ARTICLE *in* JOURNAL OF PHYSICAL CHEMISTRY LETTERS · NOVEMBER 2015

Impact Factor: 7.46 · DOI: 10.1021/acs.jpclett.5b01865

CITATION

1

READS

52

## 4 AUTHORS, INCLUDING:



**Yajie(Jessica) Jiang**

University of New South Wales

9 PUBLICATIONS 7 CITATIONS

SEE PROFILE



**Arman Mahboubi Soufiani**

University of New South Wales

7 PUBLICATIONS 4 CITATIONS

SEE PROFILE



**Anita Ho-Baillie**

University of New South Wales

32 PUBLICATIONS 346 CITATIONS

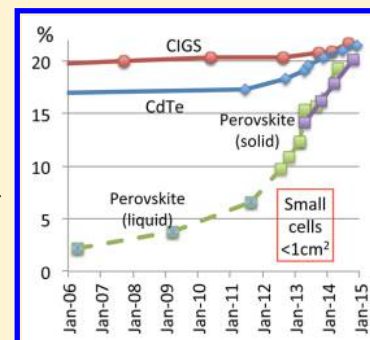
SEE PROFILE

# Optical Properties of Photovoltaic Organic–Inorganic Lead Halide Perovskites

Martin A. Green,<sup>\*</sup> Yajie Jiang, Arman Mahboubi Soufiani, and Anita Ho-Baillie

Australian Centre for Advanced Photovoltaics, School of Photovoltaic and Renewable Energy Engineering, University of New South Wales, Sydney, New South Wales 2052, Australia

**ABSTRACT:** Over the last several years, organic–inorganic lead halide perovskites have rapidly emerged as a new photovoltaic contender. Although energy conversion efficiency above 20% has now been certified, improved understanding of the material properties contributing to these high performance levels may allow the progression to even higher efficiency, stable cells. The optical properties of these new materials are important not only to device design but also because of the insight they provide into less directly accessible properties, including energy-band structures, binding energies, and likely impact of excitons, as well as into absorption and inverse radiative recombination processes.



Commercial and near-commercial solar cell technologies are dominated largely by materials where good photovoltaic performance was identified 40 years or more ago. After demonstrating initial promise, incremental improvements have allowed the 20% efficiency milestone to be exceeded in most cases after decades of research. This makes all the more surprising the rapid emergence of organic–inorganic lead halide perovskites as a new photovoltaic contender, following a more rapid and unique developmental path from these earlier successful technologies.<sup>1</sup>

The earlier technologies (e.g., Si, GaAs, CdTe,  $\text{CuIn}_x\text{Ga}_{1-x}\text{Se}_2$ ) have been almost exclusively based on classical tetrahedrally coordinated semiconductors, while the new materials involve heavier atoms, specifically Pb and I, in the perovskite structure of Figure 1a and 1b.<sup>1</sup> The perovskite can form the symmetrical cubic structure of Figure 1a if the relative ionic radii of the constituents meet a restricted range of criteria.<sup>2</sup> In particular, cation A that helps stabilize the Pb/I octahedra in position must have the largest ionic radius, larger than that of cation B in particular (Pb for these perovskites).

Although there are a small number of monovalent elemental cations with ionic radius large enough to meet this criterion, a larger group of organic cations such as the methylammonium (MA: formula  $\text{H}_3\text{CNH}_3^+$ ) and formamidinium (FA: formula  $\text{HC}[\text{NH}_2]_2^+$ ) are large enough to meet these geometrical requirements. If the cation A is slightly too small, the less symmetric orthorhombic structure of Figure 1b can form.<sup>2,3</sup> All the perovskites of photovoltaic interest form such an orthorhombic phase at low temperature, with two or more phase transitions through more symmetrical arrangements with increasing temperature, until the transition to the symmetrical cubic structure is made, generally by room temperature. Unlike the cation A shown in Figure 1, the organic cations that occupy this location do not have spherical symmetry. For the low temperature orthorhombic phase, these cations have fixed

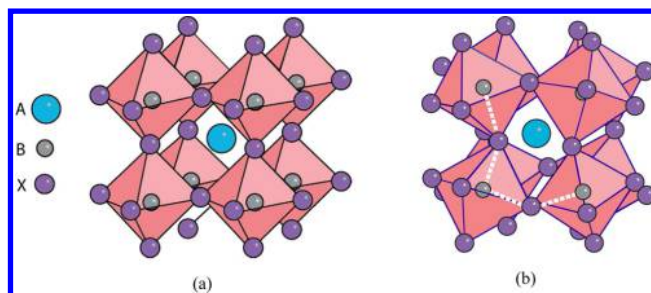


**Figure 1.** Perovskite crystal structures. (a) High temperature cubic phase. (b) Low temperature orthorhombic phase. For the perovskites of photovoltaic interest, the large cation A is generally either a methylammonium (MA) or a formamidinium (FA) cation, cation B is Pb, and anion X is a halogen (usually I, but Br and Cl are also of interest). The white dashed lines in panel b define two angles in the near-vertical (azimuthal) and near-horizontal (equatorial) planes that can be used to characterize deviations from the more symmetrical cubic geometry.<sup>5</sup>

orientations that alternate between two possibilities in adjacent sites within the crystal structure.<sup>3</sup> For the higher temperature phases, the organic cations oscillate between several different symmetrical positions within each unit cell on a picosecond time scale, thereby imparting approximate spherical symmetry to their average position.<sup>3,4</sup>

Although these perovskites have many properties that make them almost ideal for photovoltaics, including appropriate bandgap, ease of deposition, strong light absorption, low defect activity, and good carrier mobilities,<sup>1</sup> they do display another range of properties that make them less ideal (including

**Received:** August 26, 2015

**Accepted:** November 12, 2015

Although these perovskites have many properties that make them almost ideal for photovoltaics, they do display another range of properties that make them less ideal.

moisture sensitivity,<sup>6</sup> decomposition under either high temperatures<sup>7</sup> or high intensity light,<sup>8</sup> finite mobility, not only those desired for photogenerated carriers but also for lattice ions<sup>9</sup> and Pb toxicity<sup>1,10</sup>). Their emergence has been so striking and their potential so high, however, that these perovskites undoubtedly warrant prolonged investigation into ways of overcoming these deficiencies.

Although the initial focus has been on one particular hybrid perovskite, MAPbI<sub>3</sub>, with the closely related MAPbBr<sub>3</sub> of secondary interest, recent developments are shifting attention to FAPbI<sub>3</sub>, particularly mixtures of the latter with smaller portions of one or more of the former.<sup>11,12</sup> The optical properties of these and related perovskites are of considerable interest in photovoltaics not only for refining device design but also because of the insight they provide into more fundamental material properties. The present state of knowledge of these optical properties is discussed below, with an emphasis on the absorption coefficient as well as the real and imaginary components of refractive index and dielectric constant and their relation to the fundamental energy band structure of these perovskites. Luminescent properties are not discussed, although they are treated elsewhere,<sup>13–15</sup> because they are fundamentally related to absorption properties.<sup>16</sup>

**Energy Band Structure.** Many recent studies have converged upon a common understanding of the key features of the energy bandstructure in these hybrid perovskites, which were actually identified some time ago.<sup>17</sup> For MAPbI<sub>3</sub>, the valence bands are associated with in-plane 5p orbitals of the iodine atom that form antibonding states with Pb 6s orbitals. The conduction bands are associated with Pb 6p orbitals that form antibonding states with I 5p orbitals. Low energy transitions

across the bandgap essentially involve an electron excitation from the I 5p orbitals to the Pb 6p orbitals.<sup>17,18</sup> States contributed by the organic cation lie far from the band edges, with the role of this cation being largely to stabilize the perovskite structure, although influencing bandgaps by modifying values of the inorganic bond angles indicated in Figure 1b.<sup>5,19</sup>

The above long-established insights have been more recently extended by more sophisticated ab initio simulations of the electronic structure.<sup>5,18–28</sup> Although density functional theory (DFT), in combination with the local density approximation (LDA) or the generalized gradient approximation (GGA), as commonly used for such calculations, is effective in describing ground state properties, it is less effective for excited states, habitually underestimating bandgaps because it generally neglects the many-body interactions associated with transitions to these states. The exceptionally good agreement obtained between early DFT calculations and experimental bandgap values for MAPbI<sub>3</sub> and FAPbI<sub>3</sub>, consequently result from compensating deficiencies in the calculations.<sup>20</sup> However, the quality of the agreement may sometimes have encouraged over-reliance on DFT results. For example, such results have been used to support claims of an order of magnitude stronger absorption in MAPbI<sub>3</sub> than GaAs,<sup>21,22</sup> whereas experimental data suggest only a marginal advantage.<sup>1</sup>

Initial DFT calculations neglected not only the previously mentioned many-body effects responsible for the underestimation of the bandgap but also compensating effects in the form of spin–orbit coupling (SOC), significant in these perovskites due to the heavy inorganic atoms involved. Since the initial work of Even et al.,<sup>20</sup> several groups<sup>5,18,19,23–28</sup> have investigated the effect of SOC upon band properties. Its main effect is seen in the conduction band, splitting the originally triply degenerate lowermost conduction states into upper and lower bands separated by around 1 eV. This weakens fundamental optical transitions at the band edge to about a third of the strength calculated ignoring SOC.<sup>23</sup> As expected, DFT calculations with SOC included underestimate the bandgap unless corrected for many-body effects.

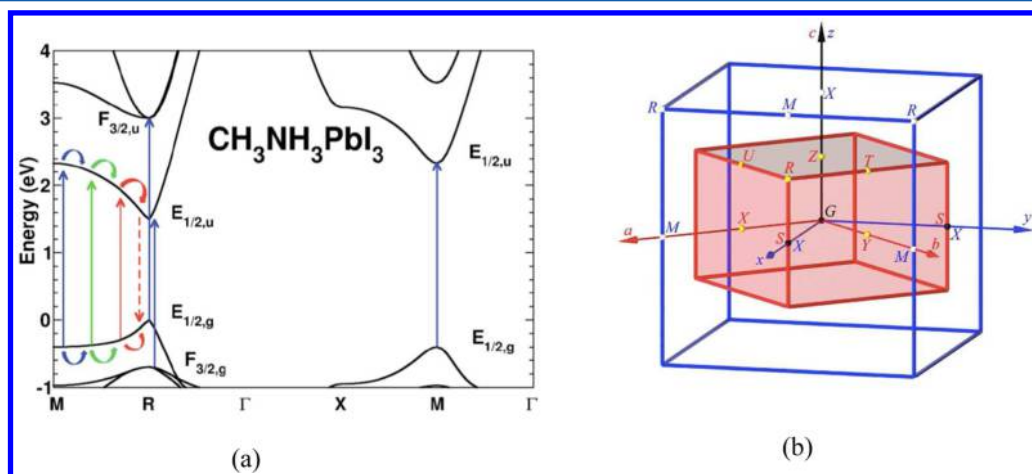


**Figure 2.** Theoretical energy band structure. (a) Calculated band structure (showing energy versus wavevector for points and lines of symmetry within the first Brillouin zone) for the cubic perovskite phase of MAPbI<sub>3</sub> including spin–orbit coupling, but with calculated conduction band energies shifted upward by 1.4 eV to match the experimental value at R. Reprinted with permission from ref 29, copyright American Chemical Society 2015. (b) Relationship between the Brillouin zones associated with the cubic (outer cuboid) and orthorhombic (inner cuboid) crystalline phases. Reprinted with permission from ref 30, copyright IOP Publishing & Deutsche Physikalische Gesellschaft. CC BY-NC-SA.

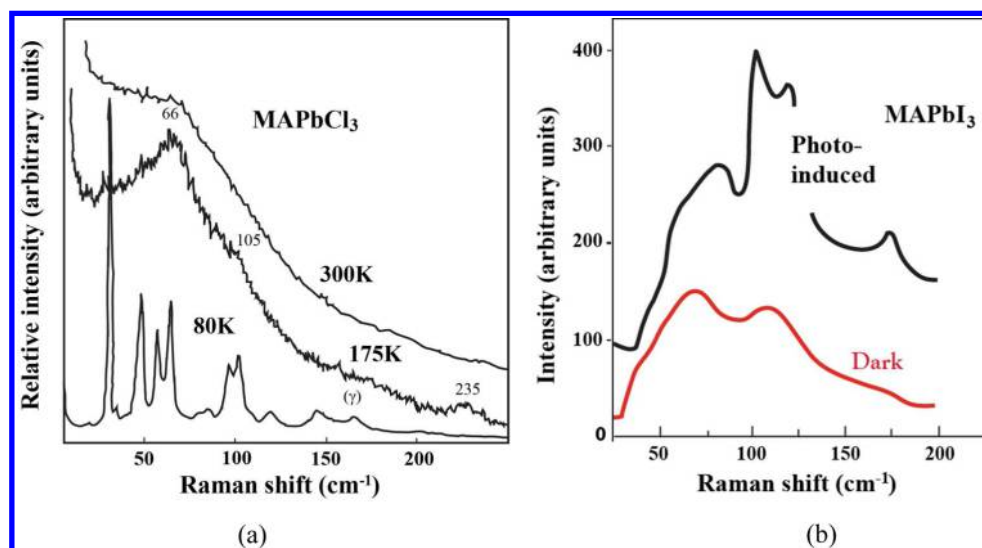


**Figure 3.** Raman spectra of organic lead halide perovskites. (a) Raman spectra of MAPbCl<sub>3</sub> in orthorhombic (lowermost), tetragonal, and cubic (uppermost) phases. Reproduced from ref 33, copyright Elsevier 1997. (b) Raman spectra of MAPbI<sub>3</sub> at room temperature after storing in the dark and after an hour of low intensity illumination. Reprinted with permission from ref 34, copyright American Chemical Society 2015.

A smaller group of calculations attempt to correct for both spin–orbit coupling and the self-energy of the electron.<sup>24–26</sup> One approach is to combine the single particle Green’s function  $G$  with the screened Coulomb interaction  $W$  in the GW approximation. Different GW approaches applied to these perovskites have recently been reviewed.<sup>26</sup> Additionally, ad-hoc corrections to the ground state DFT computation can be made with the help of hybrid DFT functionals, thus artificially reproducing electronic transition energies between the crystal ground and excited states.<sup>27</sup>

For band structure calculations, a periodic crystal structure first needs to be specified. This poses problems for these hybrid organic perovskites in their high temperature phases since the symmetry imposed is time averaged. Although the first widely used perovskite, MAPbI<sub>3</sub>, is in the tetragonal phase at room temperature, the symmetrical cubic phase (Figure 1a) has been the most widely analyzed, partly because it involves the least computational resources and partly because most of the interesting perovskites are in this phase at likely cell operating temperatures. Different approaches have been used to enforce the static spherical symmetry required to allow the analysis to proceed. One is to replace the organic cation by a Cs<sup>+</sup> cation in the analysis but use experimental spacings deduced for the organic cation.<sup>20,23</sup> Another is to remove the organic cation completely from the structural model and compensate the negative charge of the inorganic network using a positive background.<sup>5</sup> Yet another approach is to analyze with the organic cation orientated in the lowest energy position within the cubic cell<sup>24</sup> or in a series of low energy positions.<sup>28</sup>

The general results from such calculations when SOC is included are reasonably consistent when bandgaps are brought into agreement with experimental values, either by detailed calculations or by uniform energy shifts of conduction band states relative to the valence band.<sup>23,25,26,29</sup> For the high-temperature cubic phase of Figure 1a, a direct bandgap at the R point (1/2,1/2,1/2) of the cubic Brillouin zone is predicted as shown in Figure 2a, with slightly higher energy transitions also occurring close to the symmetry line from R to the M point (1/2,1/2,0). Notably, there is a large separation between the bands at the zone center  $\Gamma$  (0,0,0).

**Optical Transitions.** For the cubic phase analyzed, the lowest energy transition across the bandgap occurs at the R point, between the doubly degenerate valence band labeled  $E_{1/2,g}$  in Figure 2a<sup>29</sup> and the lower split-off conduction band labeled  $E_{1/2,u}$ . Increasing photon energy promotes excitations close to the R–M symmetry line. As the photon energy increases to about 0.7 eV above the bandgap, transitions from the second highest valence band ( $F_{3/2,g}$ ) to the lowest conduction band ( $E_{1/2,u}$ ) also become feasible. By quantifying optical matrix elements<sup>23</sup> (neglecting excitonic effects, as for the other optical transition strengths mentioned below), the strength of these transitions is calculated to be only roughly a third that of the original  $E_{1/2,g}$  transitions at R. Transitions at the saddle point M, occurring at an energy of 1.4 eV above the bandgap in Figure 2a, are calculated to be the strongest, 3–4 times stronger than the stronger of the transitions at R.

At an energy 1.6 eV above the bandgap, additional transitions from the upper valence band ( $E_{1/2,g}$ ) to the higher level split-off conduction bands ( $F_{3/2,u}$ ) become possible at R with a similar strength to the initial lowest energy transition at this point.<sup>23</sup> Finally, at an energy of 2.4 eV above the bandgap, transitions from the lower lying valence band ( $F_{3/2,g}$ ) to this band ( $F_{3/2,u}$ ) also become possible, with about half the previously mentioned strength,<sup>23</sup> although at this energy, transitions at many other regions within the Brillouin zone are also possible. Other calculations of the energies for the transitions mentioned (in the cubic phase including SOC) are in good agreement when taken relative to the fundamental transition, although the energy calculated for the second valence band below the first varies between calculations from 0.55 to 1.2 eV,<sup>24,25</sup> rather than having the value of 0.8 eV shown in Figure 2a, correspondingly altering the energies of the transitions associated with this band.

Although the orthorhombic structure is only relevant at low temperatures, calculation of the corresponding bandstructure involves fewer assumptions because the organic cations are in ordered positions in this phase, making this structure also the focus of several studies with SOC included.<sup>27–29</sup> The gross features of the resulting bandstructure can be deduced by folding the features of Figure 2a calculated for the cubic geometry into the reduced Brillouin zone corresponding to the



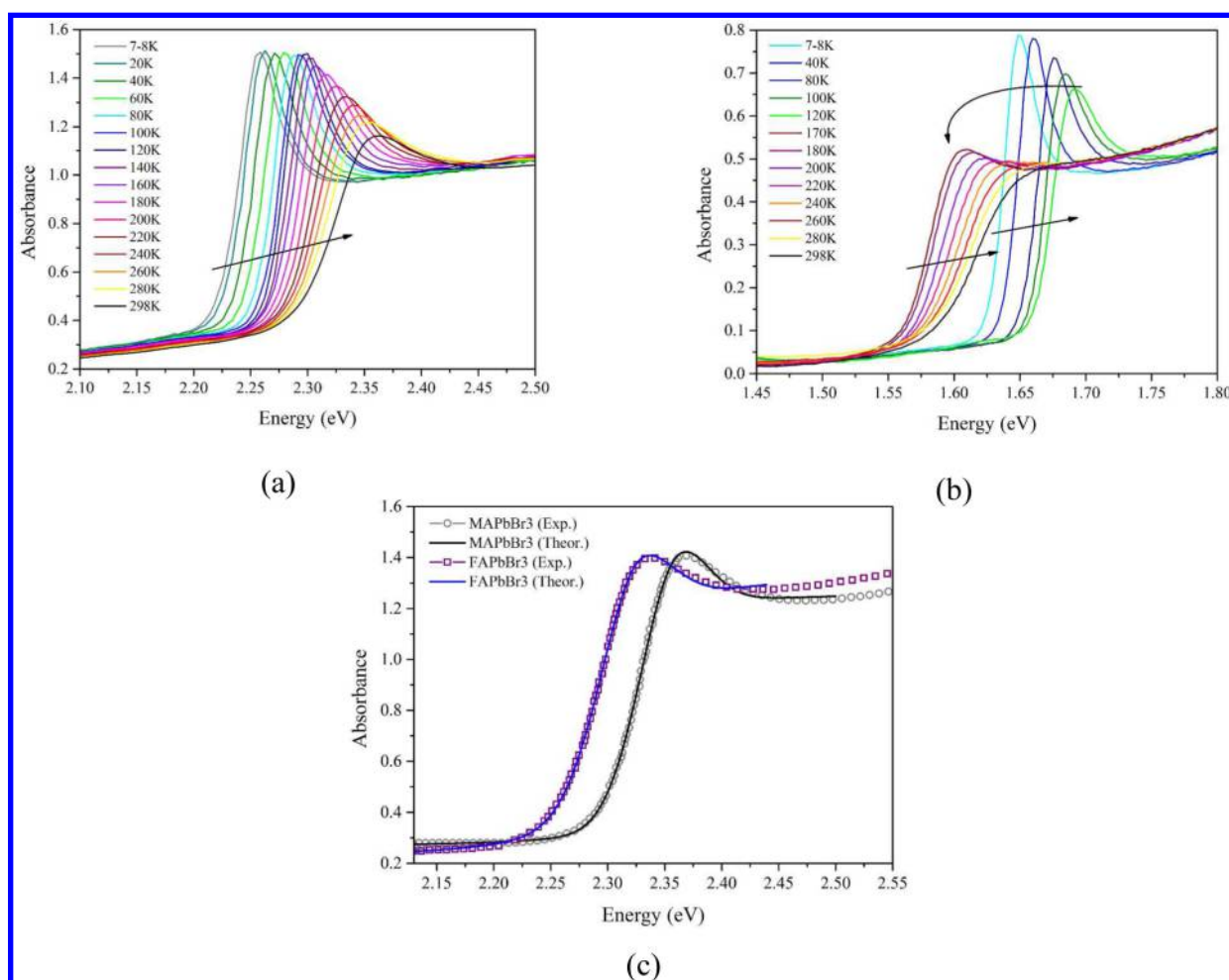


**Figure 4.** Absorbance measurements of several organic lead perovskite samples. (a) MAPbBr<sub>3</sub> over a wide temperature range;<sup>40</sup> (b) MAPbI<sub>3</sub> also over a wide temperature range;<sup>40</sup> (c) MAPbBr<sub>3</sub> and FAPbBr<sub>3</sub> at room temperature (reprinted with permission from ref 41, copyright American Chemical Society 2014), including a theoretical fit discussed in the text.

four times larger unit cell associated with the orthorhombic structure as shown in Figure 2b ( $Z = 4$ , where  $Z$  is the number of formula units per unit cell). Features at the  $\Gamma$  zone center in the cubic case remain at  $\Gamma$ , whereas band-folding reflects features at R, M, and X also to  $\Gamma$ , resulting in an apparent 4-fold increase in the number of bands.<sup>31,32</sup> Alternatively, Figure 2a can be regarded as an approximate extended zone representation of the orthorhombic structure with not only vertical optical transitions allowed but also those involving a change of wavevector equal to the now smaller reciprocal lattice vector.

Similar effects also occur for higher temperature tetragonal phases also with  $Z = 4$ . Although there are some additional effects in these noncubic phases due to bond distortions as well as band-crossing effects,<sup>32</sup> the simpler picture arising from the cubic phase remains of interest for several reasons. One is that the more complex bandstructures of the less symmetrical phases can be related to those in the cubic phase by bandfolding or lattice vector conserving transitions as noted above. A second is that technological interest is shifting to material in the cubic phase with the growing interest in FAPbI<sub>3</sub> and its alloys. Even MAPbI<sub>3</sub>, in the tetragonal phase at room temperature, is in the cubic phase at likely cell operating temperatures, and additionally, cubic phase alloys with MAPbBr<sub>3</sub> are of interest due to greater moisture tolerance.

As noted, the analyses of the high temperature phases of most practical interest are approximate due to the need to model a time-averaged symmetry. A much larger unit cell would be required to capture the diversity represented by random organic cation orientation between a set of discrete options. One might expect that this would result in more bandfolding and more allowed transitions within a much smaller Brillouin zone associated with the increased unit cell size. Another way of expressing this expectation is that the random orientation of the organic cation might be expected to destroy translational symmetry, relaxing the need for wavevector conservation during optical transitions.

There is strong evidence for this lack of translational symmetry for high temperature phases of MAPbCl<sub>3</sub>.<sup>33</sup> Figure 3 shows Raman signals measured at 80, 175, and 300 K when the material is expected to be in its orthorhombic, tetragonal, and cubic phases, respectively. In the orthorhombic phase, the Raman signal has many peaks corresponding to interactions of the incident light with wavevector conserving phonons of the required symmetry (24 allowed Raman active phonon modes for similar inorganic orthorhombic perovskites<sup>35</sup>). In the tetragonal phase, eight Raman active modes could be expected for an inorganic perovskite.<sup>33</sup> However, on transitioning to this phase (175 K curve), the clearly resolved peaks in the orthorhombic phase of MAPbCl<sub>3</sub> are replaced by a much less

structured spectrum with evidence only for broad peaks at wavevectors of 66, 105, and 235  $\text{cm}^{-1}$  in the range shown. This is consistent with the loss of translational symmetry with phonons from across the Brillouin zone consequently able to contribute to scattering of the incident light. An ideal cubic perovskite has no Raman active modes.<sup>35</sup> However, MAPbCl<sub>3</sub> in the cubic phase at 300 K maintains a broad response similar to that observed for the tetragonal phase suggesting phonons from the entire Brillouin zone are Raman active as expected in the absence of translational symmetry. If wavevector conservation does not apply to Raman scattering, formally involving optical excitations through virtual electronic states, might not the same be expected to apply to optical transitions realized as actual rather than virtual?

The actual situation is more subtle<sup>36</sup> and has been investigated in detail for random semiconductor alloys.<sup>37,38</sup> When frozen in time, the random orientation of the organic cations would create disturbances to the lattice periodicity and potentials similar to the random placement of different atoms at lattice sites within a III–V semiconductor alloy system. The approach generally adopted is to treat semiconductor alloys in the same way as a pure crystal, using a well-defined wavevector in the reduced Brillouin zone corresponding to that of the pure crystal, within the framework of a virtual crystal approximation (VCA).<sup>39</sup> In this approach, atoms in the crystal are replaced by “artificial” atoms with properties intermediate between the different atoms forming the alloy. It is nonetheless understood that deficiencies in the VCA approach make the alloy different from pure semiconductor in some important aspects. Among these include prospects for direct absorption across an indirect gap, line width broadening in optical transitions, and a reduction in carrier mobility.<sup>37</sup> Increasing sophistication in solving large supercells containing thousands or even hundreds of thousands of atoms is providing more insight into the appropriateness of a Brillouin zone representation of alloy properties.<sup>37,38</sup> For gentle perturbations, this representation seems appropriate. The random orientations of organic cations within these perovskites produce relatively modest perturbations in bandgaps and energy alignments<sup>33</sup> compared with even the better matched of the III–V semiconductor alloy systems that have been studied. The strong SOC also reduces the impact of local lattice distortions upon the electronic states involved in optical absorption.<sup>20</sup>

Interestingly, for MAPbI<sub>3</sub> in the disordered tetragonal phase at room temperature, there have been recent reports of a reversibly increased organic cation alignment, restoring translational symmetry, after prolonged exposure to low intensity light.<sup>34</sup> The evidence for this is the increasing amount of well-defined structure that becomes apparent in the Raman spectrum, as shown in Figure 3b.

**Absorption Properties.** The optical properties most directly related to the bandstructure discussed above are the light absorption properties, as often surveyed in simple absorbance measurements (absorbance =  $-\log T$ , where  $T$  is the fractional transmission of a layer of the material). Such measurements are useful in identifying the key optical features, such as the absorption edge. Figure 4a shows absorbance measurements for a MAPbBr<sub>3</sub> film over a wide range of temperatures.<sup>40</sup> A strong excitonic peak signals the onset of strong absorption, with this peak broadening with increased temperature and with the absorption edge also shifting monotonically to higher energies as the temperature increases. This bandgap variation is the opposite of the behavior of normal tetrahedrally coordinated

semiconductors and is attributed to the antibonding nature of the highest energy valence band states in these perovskites.

Note that, at energies higher than the excitonic peak, there is only a weak dependence of absorbance on temperature, despite MAPbBr<sub>3</sub> undergoing a phase change from orthorhombic to tetragonal at around 145 K, and from a second tetragonal phase to cubic at 237 K.<sup>42</sup> This is regardless of the fact that translational symmetry is expected to prevail in the orthorhombic phase, although not in the higher temperature phases, suggesting the different band-folding effects and the loss of translational symmetry do not have a large impact on the strength of optical properties, at least near the band edge.

Similar measurements on MAPbI<sub>3</sub> films (Figure 4b) show some similarities and contrasts. Again, there is a trend to higher bandgap with increasing temperature, but with a sudden bandgap decrease of ca. 100 meV between 120 and 170 K due to the orthorhombic to tetragonal phase transition in this material. The bandgap decrease at the transition is in the direction expected from the decreased bond angle distortion in the tetragonal phase,<sup>5</sup> although a similar decrease is not apparent for MAPbBr<sub>3</sub>.

Figure 4c shows the change in absorption edge reported on changing the organic cation in the bromide from MA to FA.<sup>41</sup> The solid lines show a theoretical fit to these data based on the excitonic absorption edge theory of Elliott.<sup>43</sup> From such fits, values of the excitonic binding energy,  $E_x$ , and bandgap,  $E_g$ , can be deduced. Room temperature values deduced from Figure 4 and results published elsewhere<sup>12</sup> are shown in Table 1. The

**Table 1. Room Temperature Bandgap  $E_g$  and Excitonic Binding Energy for Some Common Perovskites Deduced from Fits to Data of Figure 4<sup>a</sup>**

	MAPbI <sub>3</sub>	FAPbI <sub>3</sub>	MAPbBr <sub>3</sub> (Figure 4a)	MAPbBr <sub>3</sub> (Figure 4c)	FAPbBr <sub>3</sub>
$E_g$ (meV)	1646	1566	2392	2384	2351
$E_x$ (meV)	12.3	8.4	36.3	30.9	31.8

<sup>a</sup>Except for FAPbI<sub>3</sub>, based on fit to data published elsewhere.<sup>12</sup>

values deduced are reasonably consistent with recently reported values using a different experimental technique<sup>44</sup> but are higher than values calculated using static dielectric constants.<sup>45</sup> Use of a Tauc plot to determine  $E_g$  from a fit to the band edge<sup>12</sup> has no theoretical basis in the presence of even modest excitonic effects, although it provides a consistent way of measuring the absorption threshold. Instead, Tauc plots will measure ( $E_g - E_x$ ) minus a broadening parameter. The absorption strength deduced from such a fit is an order of magnitude higher than the theoretical value for unbound carrier absorption that a Tauc plot models. Note that the difference between the values for  $E_g$  and  $E_x$  deduced using the Elliot theory for MAPbBr<sub>3</sub> using data from two different sources gives an indication of the scatter typically seen with the present data extraction approach.

Use of a Tauc plot to determine  $E_g$  has no theoretical basis in the presence of even modest excitonic effects, although it provides a consistent way of measuring the absorption threshold.

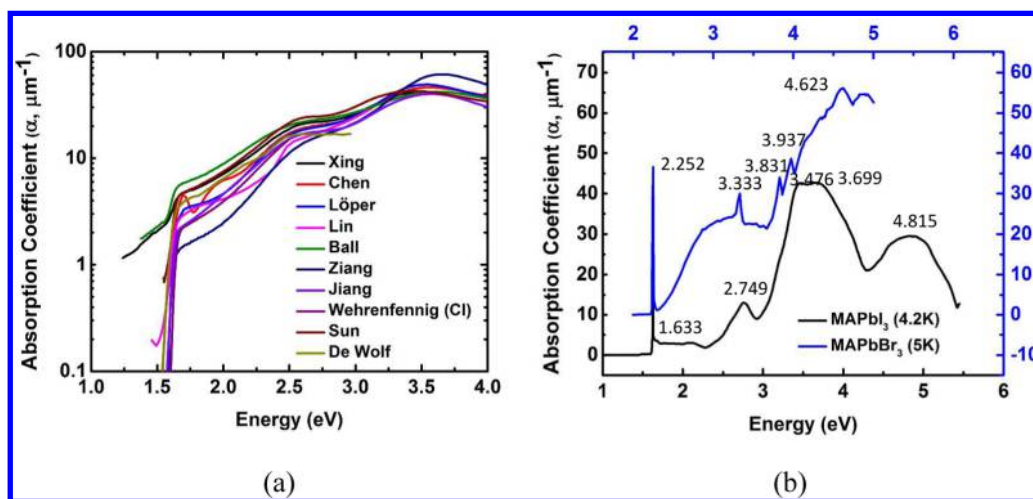


**Figure 5.** Absorption coefficients. (a) Compilation of room temperature absorption coefficient data for MAPbI<sub>3</sub> and MAPbI<sub>3</sub>(Cl). (b) Low temperature absorption coefficient of MAPbI<sub>3</sub> (4.2 K)<sup>56</sup> and MAPbBr<sub>3</sub> (5 K),<sup>57</sup> with the latter shifted by 619 meV to lower energy in energy to highlight common features (Data sources are Xing,<sup>48</sup> Chen,<sup>49</sup> Löper,<sup>50</sup> Lin,<sup>45</sup> Ball,<sup>51</sup> Ziang,<sup>52</sup> Jiang,<sup>53</sup> Wehrenfennig,<sup>54</sup> Sun,<sup>55</sup> and De Wolf<sup>46</sup>).

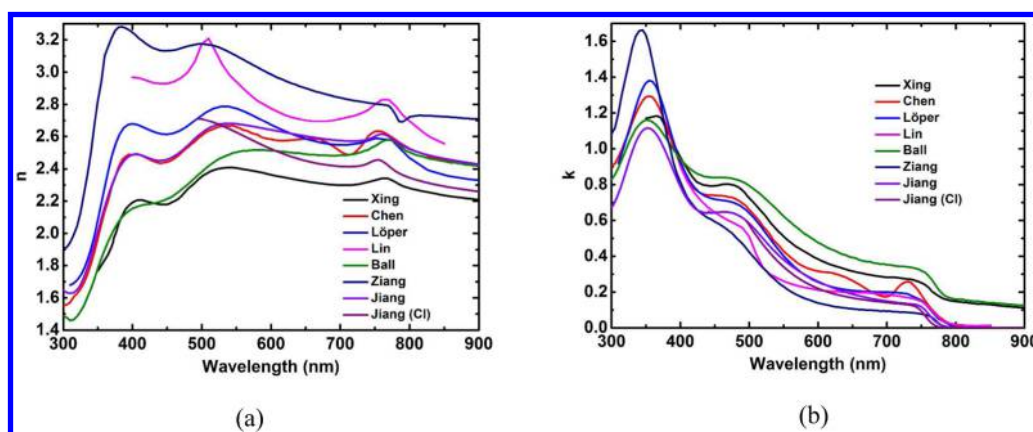


**Figure 6.** Published room temperature  $n$  and  $k$  optical index data for MAPbI<sub>3</sub>, including for some samples with small amounts of Cl. (a)  $n$ , with data sources identified in Figure 5; (b)  $k$ .

Absorption coefficients ( $\alpha$ ) for these perovskites also can be extracted from such absorbance data taking into account the effect of reflection. An independent approach is via spectroscopic ellipsometry (SE) whereby optical constants are extracted from polarized reflection from the materials involved. Photothermal deflection spectroscopy (PDS) is another technique for direct absorption coefficient measurement.<sup>46,47</sup>

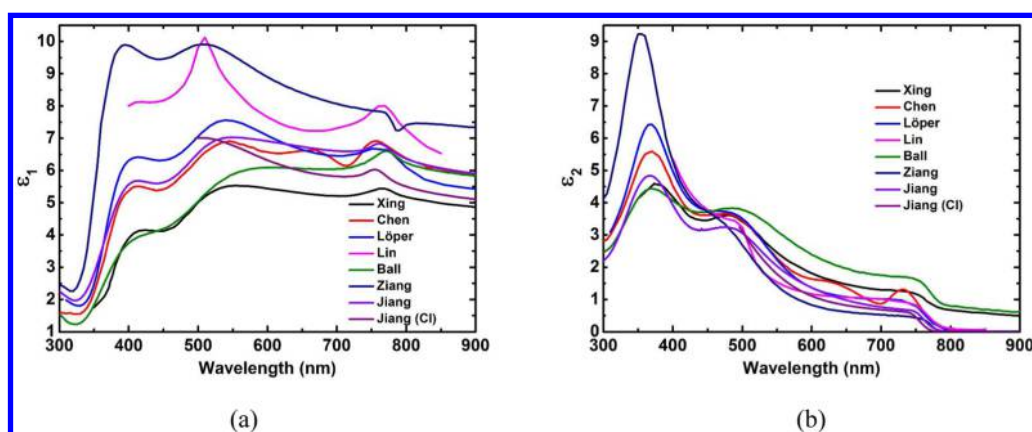
A compilation of absorption coefficient data measured at room temperature for MAPbI<sub>3</sub> (including material with a small percentage of Cl) is shown in Figure 5a.<sup>45,46,48–55</sup> Immediately obvious is the widespread variation in reported values, as well as distinctive features common to most of the reported data. As an example of the spread, at 2.0 eV, reported  $\alpha$  values range from 2.5 to 8.9/ $\mu\text{m}$ , whereas common features are an absorption edge at 1.6 eV, a hump in the characteristics at 2.5 eV and a peak in  $\alpha$  at around 3.5 eV, with the spread in the  $\alpha$  value at this peak considerably decreased, ranging from 40 to 49/ $\mu\text{m}$ , with one outlier at 61/ $\text{cm}$ .

Some SE data show high  $\alpha$  even below the band edge, suggesting ellipsometry may not be accurate for low  $\alpha$  values, because it is prone to errors arising from the different assumptions made and models used in fitting the data. Better agreement is obvious at higher energies. One data set has additional humps not seen in other data, likely to be a

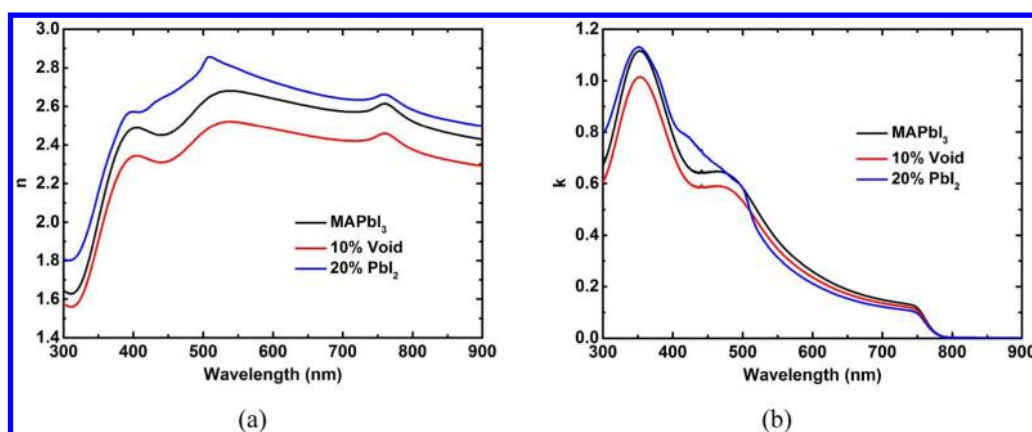
measurement artifact. A plot showing the relation of perovskite values to those of other materials of interest in photovoltaics has been reported elsewhere,<sup>1</sup> with  $\alpha$  values similar to those of GaAs, InP, and CdTe.

Figure 5b shows  $\alpha$  deduced from reflection from single crystals at liquid helium temperatures<sup>56,57</sup> for both MAPbI<sub>3</sub> and MAPbBr<sub>3</sub>, with the energy scale shifted to highlight common features. The strong excitonic peaks of Figure 4a and b at the absorption edge are even more apparent on the condensed energy scale. Although bound Wannier excitons with relatively high binding energy have been tentatively identified in the orthorhombic phase based on low temperature photoluminescence studies,<sup>58</sup> corresponding features are not expected to be readily apparent in inverse absorption coefficient measurements due to this large binding energy.<sup>16</sup> A second possibly excitonic peak is observed at an energy  $1.10 \pm 0.02$  eV higher in both cases. In view of this common value and its good agreement with theoretical expectations, this is attributed to the onset of transitions to the higher energy spin orbit split-off conduction bands. Both curves show a strong increase in absorption at an energy of 1.4 eV above the bandgap that might be associated with transitions at the M point (or its reflection) or with the large increase in states within the valence band at such energies.





**Figure 7.** Real ( $\epsilon_1$ ) and imaginary ( $\epsilon_2$ ) parts of the room temperature dielectric constant of MAPbI<sub>3</sub>, including for some samples with small amounts of Cl. (a) Real,  $\epsilon_1$ ; (b) imaginary,  $\epsilon_2$  (data sources are identified in Figure 5).



**Figure 8.** Effect of moderate amounts of voids and PbI<sub>2</sub> upon the refractive index of MAPbI<sub>3</sub> at room temperature. (a) Effect on  $n$  data; (b) Effect on  $k$  of ref 53

Very recent work<sup>59,60</sup> has attempted a more definite assignment using critical point analysis. Although this has been a good start on increased sophistication in assigning optical features, relating experimental to theoretical features is complicated by the general neglect of excitonic effects in the latter that considerably enhance the strength of optical processes.

**Complex Refractive Index.** Despite an earlier dearth of information, there have been several recent publications reporting values of the real and imaginary parts of the refractive index ( $n$  and  $k$ , respectively) for MAPbI<sub>3</sub> with results shown in Figure 6. Also shown in Figure 7 are the corresponding values of the real and imaginary parts of the dielectric constant, directly related to the refractive indices ( $\epsilon_1 = n^2 - k^2$ ;  $\epsilon_2 = 2nk$ ). Immediately obvious again is the spread in published values, appreciably larger than observed for traditional semiconductors.

There may be several reasons for this. One is that several measurements are based on extracting parameters for layers embedded in device structures, with the accuracy of perovskite parameter extraction dependent on the accuracy of modeling the optical properties of companion layers. Another is that some deposition approaches are known to produce layers of nonuniform thickness, often including voids. A third is that samples with similar chemical composition fabricated following similar procedures can produce different grain size distributions<sup>61</sup> affecting extracted values due to effects such as different levels of scattering. Furthermore, these perovskites may not be

single-phase as assumed, but two-phase material involving PbI<sub>2</sub>, incorporated either during material preparation or as a byproduct from material degradation over time or as a result of exposure to high temperature or high light intensities. Another contributor may be material anisotropy since some preparation techniques produce highly orientated material, whereas others produce more random structures,<sup>62</sup> although anisotropic effects are expected to be small.

Figure 8 shows the effects of an appreciable fraction of voids and PbI<sub>2</sub> upon likely measured values, based on effective medium calculations. Voids that are present but are unaccounted for in data extraction are likely to result in extracted  $n$  and  $k$  values that are both uniformly low across the spectrum. There are no clear examples of this in Figure 6, except possibly the Jiang (Cl) sample.<sup>53</sup> Lowest values of  $n$  in Figure 6 instead tend to be correlated with high values of  $k$ .

The effect of PbI<sub>2</sub>, also shown in Figure 8, is more subtle. Reasonable amounts of PbI<sub>2</sub> in the form of small precipitates are likely to increase  $n$  at all wavelengths (Figure 8a) and to sharpen the peak around 500 nm (2.5 eV) when PbI<sub>2</sub> becomes strongly absorbing. The effect of PbI<sub>2</sub> upon  $k$  is to decrease at long wavelengths while tending to remove the plateau in the 400–500 nm range that is apparent in many data sets (Figure 8b) by increasing  $k$  at short wavelengths. One data set in Figure 6 shows both these distinctive features suggesting the sample measured had a high concentration of small PbI<sub>2</sub> precipitates.



Other curves in Figure 6 show additional unusual features that gives most confidence in the “middle of the road” data presented by Jiang et al.<sup>53</sup> and Löper et al.,<sup>50</sup> with the corresponding permittivities also appearing the most reasonable.

Despite the enormous diversity possible, optical properties on any material are limited by nature, with fundamental interconnections captured by the Kramers–Kronig (KK) relationships.

**Sum Rules.** Despite the enormous diversity possible, optical properties on any material are rigorously limited by nature,<sup>63</sup> with fundamental interconnections captured by the Kramers–Kronig (KK) relationships. In terms of the dielectric constant, the KK relations become<sup>63</sup>

$$\varepsilon_1(\omega) = 1 + \frac{2}{\pi} P \int_0^\infty \frac{\omega' \varepsilon_2(\omega')}{(\omega')^2 - \omega^2} d\omega' \quad (1)$$

$$\varepsilon_2(\omega) = -\frac{2\omega}{\pi} P \int_0^\infty \frac{\varepsilon_1(\omega')}{(\omega')^2 - \omega^2} d\omega' \quad (2)$$

where  $P$  represents the Cauchy principle value of the integral (an essential subtlety since the integrand is infinite when  $\omega' = \omega$ ). Identical relationships hold if  $\varepsilon_1$  is replaced by  $n$  while  $\varepsilon_2$  is replaced by  $k$ . Because the results are dimensionless, the radial frequency  $\omega$  in the above equations can be replaced by other units proportional to energy, such as photon energy  $E$  itself. Despite the great generality and power of these relationships, they are imposing due to the embodied singularity and can be difficult to use, because values of  $\varepsilon_1$  or  $\varepsilon_2$ ,  $n$  or  $k$  need to be known over the whole frequency range, in principle, to apply them.

Some simplification occurs if there is an interest in semiconductor properties at wavelengths below the bandgap where there is a range of photon energies  $E_L < E_{tr} < E_H$  where the semiconductor is transparent (both  $\varepsilon_2$  and  $k$  approximately = 0). Hence

$$\begin{aligned} \varepsilon_1(E_{tr}) &= 1 + \frac{2}{\pi} \int_0^{E_L} \frac{E \varepsilon_2(E)}{E^2 - E_{tr}^2} dE + \frac{2}{\pi} \int_{E_H}^\infty \frac{E \varepsilon_2(E)}{E^2 - E_{tr}^2} dE \\ &= 1 - \frac{2}{\pi E_{tr}^2} \int_0^{E_L} E \varepsilon_2(E) \left[ \sum_{n=0}^\infty \left( \frac{E}{E_{tr}} \right)^{2n} \right] dE \\ &\quad + \frac{2}{\pi} \int_{E_H}^\infty \frac{\varepsilon_2(E)}{E} \left[ \sum_{n=0}^\infty \left( \frac{E}{E_{tr}} \right)^{2n} \right] dE \end{aligned} \quad (3)$$

The lower and upper  $j$ th moments of  $\varepsilon_2$  (a material constant) can be defined as

$$\begin{aligned} M_j^L(\varepsilon_2) &= \frac{2}{\pi} \int_0^{E_L} E^j \varepsilon_2(E) dE \\ M_j^H(\varepsilon_2) &= \frac{2}{\pi} \int_{E_H}^\infty E^j \varepsilon_2(E) dE \end{aligned} \quad (4)$$

Then, for  $E_L < E < E_H$ , eq 3 becomes

$$\varepsilon_1(E) = 1 - \sum_{j=0}^\infty [M_{2j+1}^L/E^{2(j+1)}] + \sum_{j=1}^\infty [E^{2(j-1)} M_{-2j+1}^H] \quad (5)$$

A similar expression holds for  $n$  in terms of moments of  $k$ . The negative term corresponds to weak sub-bandgap absorption processes, such as due to phonon absorption, and is generally negligible at near-infrared frequencies. Although more complex empirical relationships bearing some relationship to eq 5 are often used to characterize refractive index dispersion in the transparency region of semiconductors, Wemple and Di Domenico<sup>64</sup> proposed the simple relationship below, attempting to link the optical and chemical properties of the material

$$n^2 - 1 = E_d E_0 / (E_0^2 - E^2) \quad (6)$$

$E$  is photon energy and  $E_d$  and  $E_0$  are constants determined by selected chemical bonding and related material properties. Specifically,  $E_d = \beta N_c Z_a N_e$ , where  $N_c$  is the coordination number of the cation (in the two component system imagined),<sup>64</sup>  $Z_a$  is the chemical valency of the anion,<sup>64</sup>  $N_e$  is the effective number of valence electrons per anion,<sup>64</sup> and  $\beta$  is an empirical constant found to have the value of  $0.26 \pm 0.04$  eV for most ionic compounds and  $0.37 \pm 0.05$  eV for covalently bonded materials.<sup>64</sup>  $E_0$  is a weighted average energy for optical transitions, with a value of 1.5 times the direct bandgap  $E_{gd}$  suggested as a reasonable estimate.<sup>64</sup> For Si ( $N_c = 4$ ,  $Z_a = 4$ ,  $N_e = 8$ ,  $E_{gd} = 3.4$  eV), this gives a long wavelength value of  $n = 3.2$ , in reasonable agreement with the experimental value of 3.4. For MAPbI<sub>3</sub>, because the Pb–I bonds are important in determining the optical properties, a value of  $n = 2.5$  is calculated ( $N_c = 6$ ,  $Z_a = 1$ ,  $N_e = 8$ ,  $E_{gd} = 1.6$  eV), again in reasonable agreement with experiment (Figure 6a). Hence, the relatively low refractive index of this material compared to the more traditional inorganic photovoltaic materials stems from the low valency of the halogen anion, aided a little by the material's ionic nature, offsetting the higher cation coordination number and smaller direct bandgap. For the other organic–inorganic lead halide perovskites, the only difference in this formula will be the value of the direct bandgap  $E_{gd}$ , leading to long wavelength estimates of the value of  $n$  for MAPbBr<sub>3</sub>, FAPbI<sub>3</sub>, and FAPbBr<sub>3</sub> of 2.1, 2.5, and 2.1, respectively.

Comparing the positive terms if eqs 5 and 6 are both expanded as power series allows  $E_0$  and  $E_d$  to be expressed in terms of the previously defined moments<sup>64</sup> of  $\varepsilon_2$

$$E_0^2 = M_{-1}^H / M_{-3}^H \quad E_d^2 = (M_{-1}^H)^3 / M_{-3}^H \quad (7)$$

As shown elsewhere,<sup>64</sup> various sum rules involving optical property relationships for nonmetals when integrated cross the whole optical frequency range can be deduced from the KK equations including the following “zero sum rules”

$$\begin{aligned} 0 &= \int_0^\infty [n(\omega) - 1] d\omega \\ &= \int_0^\infty [\varepsilon_1(\omega) - 1] d\omega \\ &= \int_0^\infty \omega k(\omega) [n(\omega) - 1] d\omega \\ &= \int_0^\infty \{[n(\omega) - 1]^2 - k^2(\omega)\} d\omega \end{aligned} \quad (8)$$

Hence, the relatively low refractive index of this material compared to the more traditional inorganic photovoltaic materials stems from the low valency of the halogen anion.

The first of these integrals shows that  $n$  must be less than unity over appreciable parts of the spectrum, because  $n$  is much higher than unity at optical frequencies and below. These subunity values occur in the extreme ultraviolet and soft X-ray region of the spectrum. Once photon energies become larger than the energy associated with that of electrons in chemical bonds, the corresponding modification of electron wave functions by these bonds can often be ignored, allowing the optical constants of a compound to be obtained by summing the contributions from the individual atoms weighted by their density.<sup>65</sup>

At these EUV and X-ray energies, the optical properties of atoms are generally described by experimental scattering parameters  $f_1$  and  $f_2$ , relating measured properties to ideal free electron properties. For large photon energies,  $f_1$  approaches the actual number of electrons per atom (the atomic number), whereas  $f_2$ , representing losses, approaches zero.<sup>65</sup> The refractive index of a material at these energies is less than unity and is normally expressed as

$$n = 1 - \delta + i\beta = 1 - \frac{r_0\lambda^2}{2\pi} \sum_m n_{\text{am}}(f_{1m} - if_{2m}) \quad (9)$$

where  $r_0$  is the classical electron radius (2.818 fm),  $\lambda$  is photon vacuum wavelength,  $n_{\text{am}}$  is the atomic density of atom of type  $m$  with  $f_{1m}$  and  $f_{2m}$  the corresponding scattering factors. Figure 9a shows the value of  $\delta$  ( $= 1 - n$ ) and  $\beta$  calculated in this way for MAPbI<sub>3</sub>, using published values of  $f_1$  and  $f_2$  for the constituent elements<sup>66</sup> ( $\beta = k$ ; the change in symbol is merely to reflect common nomenclature in the EUV and optical literature). The advantage of these insights is that it allows contributions to be found from the high energy end of the integrals shown in eq 7.

As well as these required relationships between optical parameters, there are others that impose constraints on their actual magnitudes that are more fundamental than those deduced by Wemple and DiDomenico<sup>64</sup> discussed earlier. The number density of electrons contributing to the optical properties,  $N_{\text{el}}$  is fundamentally related to the resulting optical properties by a series of relationships that include the following (SI units):<sup>63</sup>

$$\begin{aligned} N_{\text{el}} &= \frac{2\varepsilon_0 m_e}{\pi} \int_0^\infty \omega \varepsilon_2(\omega) d\omega = \frac{4\varepsilon_0 m_e}{\pi} \int_0^\infty \omega k(\omega) d\omega \\ &= -\frac{2\varepsilon_0 m_e}{\pi} \int_0^\infty \omega \text{Im}[\varepsilon^{-1}(\omega)] d\omega \end{aligned} \quad (10)$$

If, instead of integrating to infinity in eq 10, the integral is truncated at a finite energy, we obtain an estimate of the number of electrons contributing to the optical properties up to that energy.<sup>63</sup> If we multiply by the volume occupied by a unit cell and divide by  $Z$ , we get the number of electrons per formula unit of the compound.

For MAPbI<sub>3</sub>, as this energy approaches infinity, we would expect this total to approach 260 electrons. Assuming this is the case, the integrals of eq 10 with finite upper energy limits can be plotted over most of the energy range with results shown in Figure 9b. By 20 eV, all 40 outer valence electrons involved in chemical bonding have made their contribution to the material optical properties. However, most of this contribution comes over the energy range from 4 to 20 eV, where there is presently little data, with only small effective numbers of these valence electrons involved in determining optical properties below 4 eV, as shown in the inset of Figure 8b. On the basis of the molecular orbital picture of the valence band composition, we would expect 2 electrons/formula unit to be associated with the uppermost Pb(6s)/I(5p) antibonding states, with only these making a strong contribution to optical properties up to 4 eV photon energy. The need for continuity in the curves shown over the 4–20 eV range places quite severe constraints on allowable values of the parameters appearing in the integrals of eq 10 over this range.

Another interesting relationship can be deduced for the value of  $n$  as  $\omega \rightarrow 0$  from the equivalent of eq 1 for  $n$

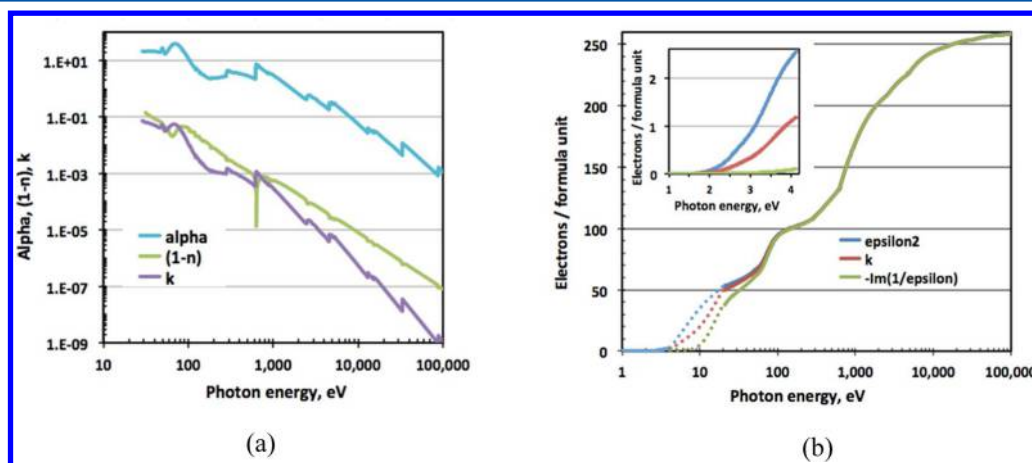


**Figure 9.** Extreme ultraviolet (EUV) and X-ray properties for MAPbI<sub>3</sub>. (a)  $\alpha$ ,  $(1-n)$  and  $k$  at high photon energies. (b) Partial sum calculation of the number of electrons per formula unit contributing to optical properties up to the photon energy indicated. The inset shows an expanded view of the low energy values. The dotted lines show regions where there is currently insufficient information to allow evaluation.

$$n_{\omega \rightarrow 0} = 1 + \frac{2}{\pi} \int_0^\infty \frac{k(\omega)}{\omega} d\omega = 1 + \frac{1}{2\pi^2} \int_0^\infty \alpha(\lambda) d\lambda \quad (11)$$

This shows that the refractive index of a material is determined by the integrated strength of absorption in the material. Within a region where the material is transparent, a similar expansion in energy to that eq 5 can be applied to  $n$  for  $E_L < E < E_H$ . Noting that  $n$  is largely energy independent in this range (Figure 6a), we can equate this nearly constant experimental value to the constant term in this expansion, giving

$$n(E_{tr}) = 1 + \frac{2}{\pi} \int_{E_g}^\infty \frac{k}{E} dE = 1 + \frac{1}{2\pi^2} \int_0^{\lambda_g} \alpha d\lambda \quad (12)$$

This shows that the infrared value of  $n$  is determined mainly by the above bandgap absorption. If we take  $E_g = 1.6$  eV and the infrared value of  $n$  as 2.25, this means that the average value of  $\alpha(\lambda)$  for  $\lambda < \lambda_g$  must be  $32/\mu\text{m}$ . Since the wavelength averaged value is less than this from 1.6 to 4.0 eV (Figure 6a) and from 20 eV to infinity (Figure 9a), it follows that the average  $\alpha$  must be higher than this in the 4–20 eV range.

**Summary and Future Directions.** The key optical features of these photovoltaically interesting organic–inorganic lead halide perovskites are a relatively low refractive index compared to traditional inorganic tetrahedrally coordinated semiconductors and a high near bandgap absorption coefficient. The low index is attributed to the low chemical valency of the halide atom while the strong band-edge absorption is due to the direct bandgap, with absorption strength similar to that of the inorganic direct bandgap semiconductors of interest to photovoltaics.

According to the Wemple–DiDomenico model,<sup>64</sup> the infrared refractive index of the organic–inorganic halide perovskites should be simply related to the bandgap via the simple relationship

$$n^2 \approx 1 + 8.32 \text{ eV}/E_g \quad (13)$$

This gives good results in the cases tested to date, producing a value of 2.5 and 2.1 for MAPbI<sub>3</sub> and MAPbBr<sub>3</sub>, respectively. The materials show an excitonic optical absorption edge, with the excitonic peaks more pronounced for the higher bandgap, lower index, and hence lower permittivity materials. Although static exciton concentrations in this material are low at room temperature due to their rapid disassociation into free carriers,<sup>67</sup> this is not inconsistent with significant enhancement of optical properties by excitons. Agreement between detailed ab initio simulations that neglect excitonic effects and experimental data is therefore not to be expected. Inclusion into such calculations is difficult due to polaronic effects expected in these ionic materials.<sup>40</sup>

Although static exciton concentrations in this material are low at room temperature, this is not inconsistent with significant enhancement of optical properties by excitons.

Even at low temperature, excitonic features at the band edge are much broader than those for traditional inorganic

semiconductors. This has been attributed to phonon interaction, although such interaction is also present for the traditional semiconductors.<sup>54</sup> Broadening may be related to the organic cation, although these are in ordered positions at low temperature. Away from the band edge, even broader peaks likely to be excitonic are detected at low temperature in both MAPbI<sub>3</sub> and MAPbBr<sub>3</sub>. This peak is located  $1.10 \pm 0.02$  eV higher in energy than the band-edge peak for both materials suggesting a common origin. This is likely the signature of the onset of absorption from the valence band maximum to the higher energy heavy-electron split-off bands in both materials. A slight difference in values might be expected due to the differences in the exciton binding energies associated with the four different transitions involved in determining this energy combined with a slight dependence of spin orbit coupling upon bonding angle.<sup>5</sup>

Past experimental measurements of absorption coefficients, complex refractive indices, and dielectric constants have produced data with values scattered over a large range. This could be due to the use of films of nonuniform thickness, the presence of voids, or the presence of Pb halide precipitates. Refinement of optical measurements to get a clearer understanding of these issues will be of interest in refining optical design of perovskite-based cells.

A clearer understanding of the relation of features observed in the optical parameters to ab initio calculations is of interest because it will allow more rigorous interrogation of the accuracy of such calculations. This will allow the development of tools that can be used with confidence as a predictor of performance of proposed material modifications, such as the replacement of Pb by a Ti/Bi combination.<sup>68</sup>

## AUTHOR INFORMATION

### Corresponding Author

\*E-mail: [m.green@unsw.edu.au](mailto:m.green@unsw.edu.au).

### Notes

The authors declare no competing financial interest.

### Biographies

**Martin Green** is currently Scientia Professor at UNSW Australia. His group's contributions to photovoltaics include development of the first 20% and 25% efficient silicon cells, first conversion of sunlight to electricity with over 40% efficiency, and commercialization of several cell technologies including the PERC cell, expected to dominate commercial cell production by 2020.

**Yajie Jiang** is currently an ARENA postdoc fellow at the University of New South Wales (UNSW). She received her Ph.D. in photovoltaics from UNSW in 2015. Her research interests focus on optical analysis of photovoltaic materials: silver for plasmonics, organic–inorganic halide perovskites, and spectrum-splitting photovoltaics.

**Arman Mahboubi Soufiani** is pursuing Ph.D. studies at the Australian Centre for Advanced Photovoltaics at UNSW Australia, commencing studies on singlet fission in organic solar cells. Currently, he works on understanding, from fundamental to device level, of optoelectronic properties of perovskite-based solar cells under the supervision of Prof. Green and Dr. Ho-Baillie.

**Anita Ho-Baillie** is a Senior Research Fellow at the Australian Centre for Advanced Photovoltaics (ACAP) at the University of New South Wales. Her research interests include perovskite solar cells including their use in tandems, high efficiency Si solar cells, group III–V on Si tandems, and manufacturing costing for photovoltaic technologies.



## ACKNOWLEDGMENTS

The Australian Centre for Advanced Photovoltaics is supported by the Australian Government through the Australian Renewable Energy Agency (ARENA). The Australian Government does not accept responsibility for the views, information or advice expressed herein.

## REFERENCES

- (1) Green, M. A.; Ho-Baillie, A.; Snaith, H. J. The Emergence of Perovskite Solar Cells. *Nat. Photonics* **2014**, *8*, 506–514.
- (2) Kieslich, G.; Sun, S.; Cheetham, K. Solid-State Principles Applied to Organic-Inorganic Perovskites: New Tricks for An Old Dog. *Chem. Sci.* **2014**, *5*, 4712–4715.
- (3) Weller, M. T.; Weber, O. J.; Henry, P. F.; Di Pumpo, A. M.; Hansen, T. C. Complete Structure and Cation Orientation in the Perovskite Photovoltaic Methylammonium Lead Iodide Between 100 and 325K. *Chem. Commun.* **2015**, *51*, 4180–4183.
- (4) Mashiyama, H.; Kurihara, Y.; Azetsu, T. Disordered Cubic Perovskite Structure of  $\text{CH}_3\text{NH}_3\text{PbX}_3$  ( $\text{X} = \text{Cl}, \text{Br}, \text{I}$ ). *J. Korean Phys. Soc.* **1998**, *32*, S156–S158.
- (5) Filip, M. R.; Eperon, E.; Snaith, H. J.; Giustino, F. Steric Engineering of Metal-halide Perovskites with Tunable Optical Band Gaps. *Nat. Commun.* **2014**, *5*, 5757.
- (6) Mosconi, E.; Azpiroz, J. M.; De Angelis, F. Ab Initio Molecular Dynamics Simulations of  $\text{MAPbI}_3$  Perovskite Degradation by Water. *Chem. Mater.* **2015**, *27*, 4885–4892.
- (7) Conings, B.; Drijkoningen, J.; Gauquelin, N.; Babayigit, A.; D'Haen, J.; D'Olieslaeger, L.; Ethirajan, A.; Verbeeck, J.; Manca, J.; Mosconi, E.; et al. Intrinsic Thermal Instability of Methylammonium Lead Trihalide Perovskite. *Adv. Energy Mater.* **2015**, *5*, 1500477.
- (8) Ledinský, M.; et al. Raman Spectroscopy of Organic-Inorganic Halideperovskites. *J. Phys. Chem. Lett.* **2015**, *6*, 401–406.
- (9) Eames, C.; Frost, J. M.; Barnes, P. R. F.; O'Regan, B. C.; Walsh, A.; Islam, M. S. Ionic Transport in Hybrid Lead Iodide Perovskite Solar Cells. *Nat. Commun.* **2015**, *6*, 7497.
- (10) Hailegnaw, B.; Kirmayer, S.; Edri, E.; Hodes, G.; Cahen, D. Rain on Methylammonium Lead Iodide Based Perovskites: Possible Environmental Effects of Perovskite Solar Cells. *J. Phys. Chem. Lett.* **2015**, *6*, 1543–1547.
- (11) Yang, W. S.; Noh, J. H.; Jeon, N. J.; Kim, Y. C.; Ryu, S.; Seo, J.; Seok, S. I. High-Performance Photovoltaic Perovskite Layers Fabricated Through Intramolecular Exchange. *Science* **2015**, *348*, 1234–1237.
- (12) Koh, T. M.; Fu, K.; Fang, Y.; Chen, S.; Sum, T. C.; Mathews, N.; Mhaisalkar, S. G.; Boix, P. P.; Baiki, T. Formamidinium-Containing Metal-Halide: An Alternative Material for Near-IR Absorption Perovskite Solar Cells. *J. Phys. Chem. C* **2014**, *118*, 16458–16462.
- (13) deQuilettes, D. W.; Vorpahl, S. M.; Stranks, S. D.; Nagaoka, H.; Eperon, G. E.; Ziffer, M. E.; Snaith, H. J.; Ginger, D. S. Impact of microstructure on local carrier lifetime in perovskite solar cell. *Science* **2015**, *348*, 683–686.
- (14) Stranks, S. D.; Burlakov, V. M.; Leijtens, T.; Ball, J. M.; Goriely, A.; Snaith, H. J. Recombination Kinetics in Organic-Inorganic Perovskites: Excitons, Free Charge, and Subgap States. *Phys. Rev. Appl.* **2014**, *2*, 034007.
- (15) Priante, D.; Dursun, I.; Alias, M. S.; Shi, D.; Melnikov, V. A.; Ng, T. K.; Mohammed, O. F.; Bakr, O. M.; Ooi, B. S. The recombination mechanisms leading to amplified spontaneous emission at the true-green wavelength in  $\text{CH}_3\text{NH}_3\text{PbBr}_3$  perovskites. *Appl. Phys. Lett.* **2015**, *106*, 081902.
- (16) Barugkin, C.; Cong, J.; Duong, T.; Rahman, S.; Nguyen, H. T.; Macdonald, D.; White, T. P.; Catchpole, K. R. Ultralow Absorption Coefficient and Temperature Dependence of Radiative Recombination of  $\text{CH}_3\text{NH}_3\text{PbI}_3$  Perovskite from Photoluminescence. *J. Phys. Chem. Lett.* **2015**, *6*, 767–772.
- (17) Papavassiliou, G. C.; Koutselas, I. B.; Terzis, A.; Whangbo, M. H. Structural and Electronic Properties of the Natural Quantum-Well System ( $\text{C}_6\text{H}_5\text{CH}_2\text{CH}_3\text{NH}_3$ ) $_2\text{SnI}_4$ . *Solid State Commun.* **1994**, *91*, 695–698.
- (18) Jishi, R. A.; Ta, O. B.; Sharif, A. D. Modeling of Lead Halide Perovskites for Photovoltaic Applications. *J. Phys. Chem. C* **2014**, *118*, 28344–28349.
- (19) Amat, A.; Mosconi, E.; Ronca, E.; Quarti, C.; Umari, P.; Nazeeruddin, M. K.; Grätzel, M.; De Angelis, F. Cation-Induced Band-Gap Tuning in Organohalide Perovskites: Interplay of Spin–Orbit Coupling and Octahedra Tilting. *Nano Lett.* **2014**, *14*, 3608–3616.
- (20) Even, J.; Pedesseau, L.; Jancu, J.-M.; Katan, C. Importance of Spin–Orbit Coupling in Hybrid Organic/Inorganic Perovskites for Photovoltaic Applications. *J. Phys. Chem. Lett.* **2013**, *4*, 2999–3005.
- (21) Yin, W.-J.; Yang, J.-H.; Kang, J.; Yan, Y.; Wei, S.-H. Halide Perovskite Materials for Solar Cells: A Theoretical Review. *J. Mater. Chem. A* **2015**, *3*, 8926–8942.
- (22) Yin, W.-J.; Shi, T.; Yan, Y. Unique Properties of Halide Perovskites as Possible Origins of the Superior Solar Cell Performance. *Adv. Mater.* **2014**, *26*, 4653–4658.
- (23) Even, J.; Pedesseau, L.; Katan, C. Analysis of Multivalley and Multibandgap Absorption and Enhancement of Free Carriers Related to Exciton Screening in Hybrid Perovskites. *J. Phys. Chem. C* **2014**, *118*, 11566–11572.
- (24) Giorgi, G.; Fujisawa, J.-I.; Segawa, H.; Yamashita, K. Small Photocurrent Effective Masses Featuring Ambipolar Transport in Methylammonium Lead Iodide Perovskite: A Density Functional Analysis. *J. Phys. Chem. Lett.* **2013**, *4*, 4213–4216.
- (25) Brivio, F.; Butler, K. T.; Walsh, A.; van Schilfgaarde, M. Relativistic Quasiparticle Self-Consistent Electronic Structure of Hybrid Halide Perovskite Photovoltaic Absorbers. *Phys. Rev. B: Condens. Matter Mater. Phys.* **2014**, *89*, 155204.
- (26) Filip, M. R.; Giustino, F. GW Quasiparticle Band Gap of the Hybrid Organic-Inorganic Perovskite  $\text{CH}_3\text{NH}_3\text{PbI}_3$ : Effect of Spin–Orbit Interaction, Semicore Electrons, and Self-Consistency. *Phys. Rev. B: Condens. Matter Mater. Phys.* **2014**, *90*, 245145.
- (27) Menéndez-Proupin, E.; Palacios, P.; Wahnón, P.; Conesa, J. C. Self-Consistent Relativistic Band Structure of the  $\text{CH}_3\text{NH}_3\text{PbI}_3$  Perovskite. *Phys. Rev. B: Condens. Matter Mater. Phys.* **2014**, *90*, 245207.
- (28) Motta, C.; El-Mellouhi, F.; Kais, S.; Tabet, N.; Alharbi, F.; Sanvito, S. Revealing the Role of Organic Cations in Hybrid Halide Perovskites  $\text{CH}_3\text{NH}_3\text{PbI}_3$ . *Nat. Commun.* **2015**, *6*, 7026.
- (29) Even, J.; Pedesseau, L.; Katan, C.; Kepenekian, M.; Lauret, J.-S.; Saponi, D.; Deleporte, E. Solid-State Physics Perspective on Hybrid Perovskite Semiconductors. *J. Phys. Chem. C* **2015**, *119*, 10161–10177.
- (30) Pavarini, E.; Yamasaki, A.; Nuss, J.; Andersen, O. K. How Chemistry Controls Electron Localization in 3d1 Perovskites: A Wannier-Function Study. *New J. Phys.* **2005**, *7*, 188 <http://iopscience.iop.org/article/10.1088/1367-2630/7/1/188/pdf>.
- (31) Even, J.; Pedesseau, L.; Katan, C.; Kepenekian, M.; Lauret, J.-S.; Saponi, D.; Deleporte, E. Solid-State Physics Perspective on Hybrid Perovskite Semiconductors. *J. Phys. Chem. C* **2015**, *119*, 10161–10177.
- (32) Katan, C.; Pedesseau, L.; Kepenekian, M.; Rolland, A.; Even, J. Interplay of Spin-orbit Coupling and Lattice Distortion in Metal Substituted 3D Tri-chloride Hybrid Perovskites. *J. Mater. Chem. A* **2015**, *3*, 9232–9240.
- (33) Maalej, A.; Abid, Y.; Kallel, A.; Daoud, A.; Lautié, A.; Romain, F. Phase Transitions and Crystal Dynamics in the Cubic Perovskite  $\text{CH}_3\text{NH}_3\text{PbCl}_3$ . *Solid State Commun.* **1997**, *103*, 279–284.
- (34) Gottesman, R.; Gouda, L.; Kalanoor, B. S.; Haltzi, E.; Tirosh, S.; Rosh-Hodesh, E.; Tischler, Y.; Zaban, A.; Quarti, C.; Mosconi, E.; et al. Photoinduced Reversible Structural Transformations in Free-Standing  $\text{CH}_3\text{NH}_3\text{PbI}_3$  Perovskite Films. *J. Phys. Chem. Lett.* **2015**, *6*, 2332–2338.
- (35) Islam, M. A.; Rondinelli, J. M.; Spanier, J. E. Normal Mode Determination of Perovskite Crystal Structures with Octahedral Rotations: Theory and Applications. *J. Phys.: Condens. Matter* **2013**, *25*, 175902.



- (36) Even, J. Pedestrian Guide to Symmetry Properties of the Reference Cubic Structure of 3D All-Inorganic and Hybrid Perovskites. *J. Phys. Chem. Lett.* **2015**, *6*, 2338–2242.
- (37) Zhang, Y.; Mascarenhas, A.; Wang, L. W. Non-Bloch Nature of Alloy States in a Conventional Semiconductor Alloy:  $\text{Ga}_x\text{In}_{1-x}\text{P}$  as An Example. *Phys. Rev. Lett.* **2008**, *101*, 036403.
- (38) Popescu, V.; Zunger, A. Extracting E Versus k Effective Band Structure from Supercell Calculations on Alloys and Impurities. *Phys. Rev. B: Condens. Matter Mater. Phys.* **2012**, *85*, 085201.
- (39) Chen, A.-B.; Sher, A. *Semiconductor Alloys: Physics and Materials Engineering*; Plenum Press: New York, 1995.
- (40) Soufiani, A. M.; Huang, F.; Reece, P.; Sheng, R.; Ho-Baillie; Green, M. A. Polaronic Exciton Binding Energy in Iodide and Bromide Organic-Inorganic Lead Halide Perovskites. *Appl. Phys. Lett.* **2015**, accepted for publication.
- (41) Hanusch, F. C.; Wiesenmayer, E.; Mankel, E.; Binek, A.; Angloher, P.; Fraunhofer, C.; Giesbrecht, N.; Feckl, J. M.; Jaegermann, W.; Johrendt, D.; et al. Efficient Planar Heterojunction Perovskite Solar Cell Based on Formamidinium Lead Bromide. *J. Phys. Chem. Lett.* **2014**, *5*, 2791–2795.
- (42) Poglitsch, A.; Weber, D. Dynamic Disorder in Methylammoniumtrihalogenoplumbates (II) Observed by Millimeterwave Spectroscopy. *J. Chem. Phys.* **1987**, *87*, 6373–6378.
- (43) Elliott, R. J. Intensity of Optical Absorption by Excitons. *Phys. Rev.* **1957**, *108*, 1384–1389.
- (44) Miyata, A.; Mitioglu, A.; Plochocka, P.; Portugall, O.; Wang, J. T.-W.; Stranks, S. D.; Snaith, H. J.; Nicholas, R. J. Direct measurement of the exciton binding energy and effective masses for charge carriers in organic–inorganic tri-halide perovskites. *Nat. Phys.* **2015**, *11*, 582.
- (45) Lin, Q.; Armin, A.; Nagiri, R. C. R.; Burn, P. L.; Meredith, P. Electro-optics of perovskite solar cells. *Nat. Photonics* **2014**, *9*, 106–112.
- (46) De Wolf, S.; Holovsky, J.; Moon, S.-J.; Löper, P.; Niesen, B.; Ledinsky, M.; Haug, F.-J.; Yum, J.-H.; Ballif, C. Organometallic Halide Perovskites: Sharp Optical Absorption Edge and Its Relation to Photovoltaic Performance. *J. Phys. Chem. Lett.* **2014**, *5*, 1035–1039.
- (47) Sadhanala, A.; Deschler, F.; Thomas, T. H.; Dutton, S. E.; Goedel, K. C.; Hanusch, F. C.; Lai, M. L.; Steiner, U.; Bein, T.; Docampo, P.; et al. Preparation of Single-Phase Films of  $\text{CH}_3\text{NH}_3\text{Pb}(\text{I}_{1-x}\text{Br}_x)_3$  with Sharp Optical Band Edges. *J. Phys. Chem. Lett.* **2014**, *5*, 2501–2505.
- (48) Xing, G.; Mathews, N.; Lim, S. S.; Yantara, N.; Liu, X.; Sabba, D.; Grätzel, M.; Mhaisalkar, S.; Sum, T. C. Low-Temperature Solution-Processed Wavelength-Tunable Perovskites for Lasing. *Nat. Mater.* **2014**, *13*, 476–480.
- (49) Chen, C. W.; Hsiao, S. Y.; Chen, C. Y.; Kang, H. W.; Huang, Z. Y.; Lin, H. W. Optical Properties of Organometal Halide Perovskite Thin Films and General Device Structure Design Rules for Perovskite Single and Tandem Solar Cells. *J. Mater. Chem. A* **2015**, *3*, 9152–9159.
- (50) Löper, P.; Stuckelberger, M.; Niesen, B.; Werner, J.; Filipič, M.; Moon, S.-J.; Yum, J.-H.; Topič, M.; De Wolf, S.; Ballif, C. Complex Refractive Index Spectra of  $\text{CH}_3\text{NH}_3\text{PbI}_3$  Perovskite Thin Films Determined by Spectroscopic Ellipsometry and Spectrophotometry. *J. Phys. Chem. Lett.* **2015**, *6*, 66–71.
- (51) Ball, J. M.; Stranks, S. D.; Horantner, M. T.; Huttner, S.; Zhang, W.; Crossland, E. J. W.; Ramirez, I.; Riede, M.; Johnston, M. B.; Friend, R. H.; et al. Optical Properties and Limiting Photocurrent of Thin-Film Perovskite Solar Cells. *Energy Environ. Sci.* **2015**, *8*, 602–609.
- (52) Ziang, X.; Shifeng, L.; Laixiang, Q.; Shuping, P.; Wei, W.; Yu, Y.; Li, Y.; Zhijian, C.; Shufeng, W.; Honglin, D.; et al. Refractive Index and Extinction Coefficient of  $\text{CH}_3\text{NH}_3\text{PbI}_3$  Studied by Spectroscopic Ellipsometry. *Opt. Mater. Express* **2015**, *5*, 29–43.
- (53) Jiang, Y.; Green, M. A.; Sheng, R.; Ho-Baillie, A. Room Temperature Optical Properties of Organic–Inorganic Lead Halide Perovskites. *Sol. Energy Mater. Sol. Cells* **2015**, *137*, 253–257.
- (54) Wehrenfennig, C.; Liu, M.; Snaith, H. J.; Johnston, M. B.; Herz, L. M. Homogeneous Emission Line Broadening in the Organo Lead Halide Perovskite  $\text{CH}_3\text{NH}_3\text{PbI}_{3-x}\text{Cl}_x$ . *J. Phys. Chem. Lett.* **2014**, *5*, 1300–1306.
- (55) Sun, S.; Salim, T.; Mathews, N.; Duchamp, M.; Boothroyd, C.; Xing, G.; et al. The Origin of High Efficiency in Low-Temperature Solution-Processable Bilayer Organometal Halide Hybrid Solar Cells. *Energy Environ. Sci.* **2014**, *7*, 399.
- (56) Hirasawa, M.; Ishihara, T.; Goto, T. Exciton features in 0-dimensional, 2-dimensional, and 3-dimensional networks of  $[\text{PbI}_6]^{4-}$  octahedra. *J. Phys. Soc. Jpn.* **1994**, *63*, 3870–3879.
- (57) Tanaka, K.; Takahashi, T.; Ban, T.; Kondo, T.; Uchida, K.; Miura, N. Comparative study on the excitons in lead–halide-based perovskite-type crystals  $\text{CH}_3\text{NH}_3\text{PbBr}_3$  and  $\text{CH}_3\text{NH}_3\text{PbI}_3$ . *Solid State Commun.* **2003**, *127*, 619–623.
- (58) Fang, H.-H.; Raissa, R.; Abdu-Aguye, M.; Adjokatse, S.; Blake, G. R.; Even, J.; Loi, M. A. Photophysics of Organic–Inorganic Hybrid Lead Iodide Perovskite Single Crystals. *Adv. Funct. Mater.* **2015**, *25*, 2378–2385.
- (59) Leguy, A. M. A.; Azarhoosh, P.; Alonso, M. I.; Campoy-Quiles, M.; Weber, O. J.; Yao, J.; et al. Experimental and theoretical optical properties of methylammonium lead halide perovskites. *Nanoscale* **2015**, DOI: 10.1039/C5NR05435D.
- (60) Shirayama, M.; Kadowaki, H.; Miyadera, T.; Sugita, T.; Kato, M.; Murata, D.; et al. Optical transitions in hybrid perovskite solar cells. 2015, *arXiv:1507.08824*. arXiv.org e-Print archive. <http://arxiv.org/abs/1507.08824> (accessed September 2015).
- (61) Egger, D. A.; Edri, E.; Cahen, D.; Hodes, G. Perovskite Solar Cells: Do We Know What We Do Not Know? *J. Phys. Chem. Lett.* **2015**, *6*, 279–282.
- (62) McLeod, J. A.; Wu, Z.; Shen, P.; Sun, B.; Liu, L. Self-Alignment of the Methylammonium Cations in Thin-Film Organometal Perovskites. *J. Phys. Chem. Lett.* **2014**, *5*, 2863–2867.
- (63) Smith, D. Y. Dispersion Theory, Sum Rules, and Their Application to the Analysis of Optical Data. In *Handbook of Optical Constants of Solids*; Palik, E. D. Ed.; Academic Press, Elsevier Inc.: Waltham, MA, 1997; Vol. 1, Ch. 3, pp 35–66.
- (64) Wemple, S. H.; DiDomenico, M. Behavior of the Electronic Dielectric Constant in Covalent and Ionic Materials. *Phys. Rev. B* **1971**, *3*, 1338–1351.
- (65) Spiller, E. *Soft X-ray Optics*; SPIE, The International Society for Optical Engineering: Bellingham, WA 1994.
- (66) Chantler, C. T.; Olsen, K.; Dragoset, R. A.; Chang, J.; Kishore, A. R.; Kotochigova, S. A.; Zucker, D. S. *X-Ray Form Factor, Attenuation and Scattering Tables*, Version 2.1 [Online]; National Institute of Standards and Technology: Gaithersburg, MD, 2005; <http://physics.nist.gov/ffast>. Originally published as Chantler, C. T. *J. Phys. Chem. Ref. Data* **2000**, *29*, 597–1048. and Chantler, C. T. *J. Phys. Chem. Ref. Data* **1995**, *24*, 71–643.
- (67) D’Innocenzo, V.; Grancini, G.; Alcocer, M. J. P.; Kandada, A. R. S.; Stranks, S. D.; Lee, M. M.; Lanzani, Snaith, H. J.; Petrozza, A. Excitons Versus Free Charges in Organo-Lead Tri-Halide Perovskites. *Nat. Commun.* **2014**, *5*, 3586.
- (68) Giorgi, G.; Yamashita, K. Alternative, Lead-free, Hybrid Organic-Inorganic Perovskites for Solar Applications: A DFT Analysis. *Chem. Lett.* **2015**, *44*, 826–828.